

Whole-cell-analysis of live cardiomyocytes using wide-field interferometric phase microscopy

Natan T. Shaked,* Lisa L. Satterwhite, Nenad Bursac, and Adam Wax

Department of Biomedical Engineering, Fitzpatrick Institute for Photonics, Duke University
Durham, North Carolina 27708, USA

*natan.shaked@duke.edu

Abstract: We apply wide-field interferometric microscopy techniques to acquire quantitative phase profiles of ventricular cardiomyocytes *in vitro* during their rapid contraction with high temporal and spatial resolution. The whole-cell phase profiles are analyzed to yield valuable quantitative parameters characterizing the cell dynamics, without the need to decouple thickness from refractive index differences. Our experimental results verify that these new parameters can be used with wide field interferometric microscopy to discriminate the modulation of cardiomyocyte contraction dynamics due to temperature variation. To demonstrate the necessity of the proposed numerical analysis for cardiomyocytes, we present confocal dual-channel fluorescence microscopy results which show that the rapid motion of the cell organelles during contraction preclude assuming a homogenous refractive index over the entire cell contents, or using multiple-exposure or scanning microscopy.

©2010 Optical Society of America

OCIS codes: (090.2880) Holographic interferometry; (180.3170) Interference microscopy; (120.5050) Phase measurement; (170.1530) Cell analysis.

References and links

1. R. H. Anderson, M. Smerup, D. Sanchez-Quintana, M. Loukas, and P. P. Lunkenheimer, "The three-dimensional arrangement of the myocytes in the ventricular walls," *Clin. Anat.* **22**(1), 64–76 (2009).
2. C. A. Walker, and F. G. Spinale, "The structure and function of the cardiac myocyte: a review of fundamental concepts," *J. Thorac. Cardiovasc. Surg.* **118**(2), 375–382 (1999).
3. S. A. Gaeta, G. Bub, G. W. Abbott, and D. J. Christini, "Dynamical mechanism for subcellular alternans in cardiac myocytes," *Circ. Res.* **105**(4), 335–342 (2009).
4. V. Salnikov, Y. O. Lukyanenko, W. J. Lederer, and V. Lukyanenko, "Distribution of ryanodine receptors in rat ventricular myocytes," *J. Muscle Res. Cell Motil.* **30**(3-4), 161–170 (2009).
5. D. L. M. Hickson-Bick, G. C. Sparagna, L. M. Buja, and J. B. McMillin, "Palmitate-induced apoptosis in neonatal cardiomyocytes is not dependent on the generation of ROS," *Am. J. Physiol. Heart Circ. Physiol.* **282**(2), H656–H664 (2002).
6. H. Satoh, L. M. Delbridge, L. A. Blatter, and D. M. Bers, "Surface:volume relationship in cardiac myocytes studied with confocal microscopy and membrane capacitance measurements: species-dependence and developmental effects," *Biophys. J.* **70**(3), 1494–1504 (1996).
7. E. U. Azeloglu, and K. D. Costa, "Cross-bridge cycling gives rise to spatiotemporal heterogeneity of dynamic subcellular mechanics in cardiac myocytes probed with atomic force microscopy," *Am. J. Physiol. Heart Circ. Physiol.* **298**(3), H853–H860 (2010).
8. A. Kamgoué, J. Ohayon, Y. Usson, L. Riou, and P. Tracqui, "Quantification of cardiomyocyte contraction based on image correlation analysis," *Cytometry A* **75**(4), 298–308 (2009).
9. E. Cuhe, P. Marquet, and C. Depeursinge, "Simultaneous amplitude-contrast and quantitative phase-contrast microscopy by numerical reconstruction of Fresnel off-axis holograms," *Appl. Opt.* **38**(34), 6994–7001 (1999).
10. P. Marquet, B. Rappaz, P. J. Magistretti, E. Cuhe, Y. Emery, T. Colomb, and C. Depeursinge, "Digital holographic microscopy: a noninvasive contrast imaging technique allowing quantitative visualization of living cells with subwavelength axial accuracy," *Opt. Lett.* **30**(5), 468–470 (2005).
11. T. Ikeda, G. Popescu, R. R. Dasari, and M. S. Feld, "Hilbert phase microscopy for investigating fast dynamics in transparent systems," *Opt. Lett.* **30**(10), 1165–1167 (2005).

12. N. T. Shaked, M. T. Rinehart, and A. Wax, "Dual-interference-channel quantitative-phase microscopy of live cell dynamics," *Opt. Lett.* **34**(6), 767–769 (2009).
13. N. T. Shaked, J. D. Finan, F. Guilak, and A. Wax, "Quantitative phase microscopy of articular chondrocyte dynamics by wide-field digital interferometry," *J. Biomed. Opt.* **15**(1), 010505 (2010).
14. N. T. Shaked, Y. Zhu, N. Badie, N. Bursac, and A. Wax, "Reflective interferometric chamber for quantitative phase imaging of biological sample dynamics," *J. Biomed. Opt.* **15**(3), 030503 (2010).
15. N. T. Shaked, T. M. Newpher, M. D. Ehlers, and A. Wax, "Parallel on-axis holographic phase microscopy of biological cells and unicellular microorganism dynamics," *Appl. Opt.* **49**(15), 2872–2878 (2010).
16. B. Rappaz, P. Marquet, E. Cucho, Y. Emery, C. Depeursinge, and P. Magistretti, "Measurement of the integral refractive index and dynamic cell morphometry of living cells with digital holographic microscopy," *Opt. Express* **13**(23), 9361–9373 (2005).
17. G. Popescu, T. Ikeda, C. A. Best, K. Badizadegan, R. R. Dasari, and M. S. Feld, "Erythrocyte structure and dynamics quantified by Hilbert phase microscopy," *J. Biomed. Opt.* **10**(6), 060503 (2005).
18. G. Popescu, Y. K. Park, W. Choi, R. R. Dasari, M. S. Feld, and K. Badizadegan, "Imaging red blood cell dynamics by quantitative phase microscopy," *Blood Cells Mol. Dis.* **41**(1), 10–16 (2008).
19. B. Rappaz, A. Barbul, Y. Emery, R. Korenstein, C. Depeursinge, P. J. Magistretti, and P. Marquet, "Comparative study of human erythrocytes by digital holographic microscopy, confocal microscopy, and impedance volume analyzer," *Cytometry A* **73**(10), 895–903 (2008).
20. R. Barer, "Interference microscopy and mass determination," *Nature* **169**(4296), 366–367 (1952).
21. G. Popescu, Y. K. Park, N. Lue, C. A. Best-Popescu, L. Deflores, R. R. Dasari, M. S. Feld, and K. Badizadegan, "Optical imaging of cell mass and growth dynamics," *Am. J. Physiol. Cell Physiol.* **295**(2), C538–C544 (2008).
22. B. Rappaz, E. Cano, T. Colomb, J. Kühn, C. Depeursinge, V. Simanis, P. J. Magistretti, and P. Marquet, "Noninvasive characterization of the fission yeast cell cycle by monitoring dry mass with digital holographic microscopy," *J. Biomed. Opt.* **14**(3), 034049 (2009).
23. F. Charrière, A. Mariani, F. Montfort, J. Kuehn, T. Colomb, E. Cucho, P. Marquet, and C. Depeursinge, "Cell refractive index tomography by digital holographic microscopy," *Opt. Lett.* **31**(2), 178–180 (2006).
24. W. Choi, C. Fang-Yen, K. Badizadegan, S. Oh, N. Lue, R. R. Dasari, and M. S. Feld, "Tomographic phase microscopy," *Nat. Methods* **4**(9), 717–719 (2007).
25. G. Popescu, Y. K. Park, K. Badizadegan, R. R. Dasari, and M. S. Feld, "Diffraction phase and fluorescence microscopy," *Opt. Express* **14**(18), 8263–8268 (2006).
26. B. Rappaz, F. Charrière, C. Depeursinge, P. J. Magistretti, and P. Marquet, "Simultaneous cell morphometry and refractive index measurement with dual-wavelength digital holographic microscopy and dye-enhanced dispersion of perfusion medium," *Opt. Lett.* **33**(7), 744–746 (2008).
27. C. L. Curl, C. J. Bellair, T. Harris, B. E. Allman, P. J. Harris, A. G. Stewart, A. Roberts, K. A. Nugent, and L. M. Delbridge, "Refractive index measurement in viable cells using quantitative phase-amplitude microscopy and confocal microscopy," *Cytometry A* **65**(1), 88–92 (2005).
28. N. Lue, W. Choi, G. Popescu, Z. Yaqoob, K. Badizadegan, R. R. Dasari, and M. S. Feld, "Live cell refractometry using Hilbert phase microscopy and confocal reflectance microscopy," *J. Phys. Chem. A* **113**(47), 13327–13330 (2009).
29. K. Edward, F. Farahi, and R. Hocken, "Hybrid shear force feedback/scanning quantitative phase microscopy applied to subsurface imaging," *Opt. Express* **17**(21), 18408–18418 (2009).
30. B. Kemper, D. Carl, J. Schneidenburger, I. Bredebusch, M. Schäfer, W. Domschke, and G. von Bally, "Investigation of living pancreas tumor cells by digital holographic microscopy," *J. Biomed. Opt.* **11**(3), 034005 (2006).
31. N. Lue, G. Popescu, T. Ikeda, R. R. Dasari, K. Badizadegan, and M. S. Feld, "Live cell refractometry using microfluidic devices," *Opt. Lett.* **31**(18), 2759–2761 (2006).
32. B. Kemper, S. Kosmeier, P. Langehanenberg, G. von Bally, I. Bredebusch, W. Domschke, and J. Schneidenburger, "Integral refractive index determination of living suspension cells by multifocus digital holographic phase contrast microscopy," *J. Biomed. Opt.* **12**(5), 054009 (2007).
33. M. Kemmler, M. Fratz, D. Giel, N. Saum, A. Brandenburg, and C. Hoffmann, "Noninvasive time-dependent cytometry monitoring by digital holography," *J. Biomed. Opt.* **12**(6), 064002 (2007).
34. V. P. Tychinsky, A. V. Kretushev, I. V. Klemayshov, T. V. Vyshenskaya, N. A. Filippova, N. T. Raikhlina, and A. A. Shtil, "Quantitative real-time analysis of nucleolar stress by coherent phase microscopy," *J. Biomed. Opt.* **13**(6), 064032 (2008).
35. N. Badie, L. Satterwhite, and N. Bursac, "A method to replicate the microstructure of heart tissue *in vitro* using DTMRI-based cell micropatterning," *Ann. Biomed. Eng.* **37**(12), 2510–2521 (2009).
36. N. Badie, and N. Bursac, "Novel micropatterned cardiac cell cultures with realistic ventricular microstructure," *Biophys. J.* **96**(9), 3873–3885 (2009).
37. N. T. Shaked, Y. Zhu, M. T. Rinehart, and A. Wax, "Two-step-only phase-shifting interferometry with optimized detector bandwidth for microscopy of live cells," *Opt. Express* **17**(18), 15585–15591 (2009).
38. W. J. Conover, *Practical Nonparametric Statistics*, 3rd Edition (John Wiley, 1999), pp. 271–276.
39. J. W. Covell, J. Ross, Jr., E. H. Sonnenblick, and E. Braunwald, "Comparison of the force-velocity relation and the ventricular function curve as measures of the contractile state of the intact heart," *Circ. Res.* **19**(2), 364–372 (1966).

40. H. S. Bader, "Effect of hypothermia on the contractile "capacity" of the myocardium," *J. Thorac. Cardiovasc. Surg.* **53**(5), 651–656 (1967).
 41. E. Marbán, "Cardiac channelopathies," *Nature* **415**(6868), 213–218 (2002).
 42. J. Engel, A. J. Sowerby, S. A. Finch, M. Fechner, and A. Stier, "Temperature dependence of Ca^{2+} wave properties in cardiomyocytes: implications for the mechanism of autocatalytic Ca^{2+} release in wave propagation," *Biophys. J.* **68**(1), 40–45 (1995).
 43. Y. Fu, G.-Q. Zhang, X.-M. Hao, C.-H. Wu, Z. Chai, and S.-Q. Wang, "Temperature dependence and thermodynamic properties of Ca^{2+} sparks in rat cardiomyocytes," *Biophys. J.* **89**(4), 2533–2541 (2005).
 44. M. Takano, T. P. Terada, and M. Sasai, "Unidirectional Brownian motion observed in an *in silico* single molecule experiment of an actomyosin motor," *Proc. Natl. Acad. Sci. U.S.A.* **107**(17), 7769–7774 (2010).
-

1. Introduction

Heart failure, the leading cause of death in the western world, is strongly linked with genetic and environmental factors. The human heart beats approximately 100,000 times a day by the action of cardiomyocytes (or myocardial cells), the contractile elements of the heart muscle. By coordinated contraction, these cells control blood flow through the blood vessels of the circulatory system [1]. The contractile apparatus within cardiomyocytes includes myofibrils composed of sarcomeres, highly-ordered arrays of myosin, actin, and numerous structural and regulatory proteins. In addition, these cells contain one or two nuclei, numerous mitochondria, and extensive junctional complexes which serve to propagate signals for contraction in synchrony [2,3]. During the cardiomyocyte contraction, the entire cell changes its three-dimensional shape rapidly, with meaningful intermediate events taking place on the millisecond time scale.

Since cardiomyocytes, as well as many other types of biological cells, are mostly-transparent entities, the amplitude of the light which interacts with them is minimally affected; thus it is hard to quantitatively interpret images of these cells obtained by conventional intensity-based light microscopy. Previous methods of imaging cardiomyocytes include electron microscopy of fixed cells [4]; exogenous contrast-agent-based imaging methods such as fluorescence microscopy [5,6]; scanning imaging methods (in which fast dynamic phenomena might be lost due to the scan time) such as confocal microscopy [6] and atomic force microscopy [7]; as well as inherently qualitative phase microscopy methods, such as phase contrast and differential interference contrast microscopy [8].

Wide-field digital interferometry (WFDI) is a quantitative holographic approach [9] that is capable of capturing the entire complex field distribution (amplitude and phase) associated with a sample in a single digital camera exposure, without the need for scanning or contrast agents. Valuable information regarding the three-dimensional structure of live cells can be obtained by using WFDI to capture the phase of the light transmitted through cells [10]. Single-exposure WFDI is especially useful for acquiring fast cell dynamics, such as the spatial transients occurring during the contraction of cardiomyocytes, since the interferometric acquisition rate can be equal to the maximal digital-camera frame rate. WFDI has been used to image various types of biological cells and dynamic cell phenomena [11–15].

Although WFDI is a quantitative recording technique, simple quasi-three-dimensional holographic visualization of the cell phase profile need not be the end of the process. Quantitative analysis permits extraction of numerical parameters which are useful for cytology or medical diagnosis. When using a transmission-mode interferometric setup for quantitative phase imaging, the resulting phase profile is proportional to the optical path delay (OPD) profile of the cell. The OPD is defined as the product of the geometric path delay (or thickness) profile of the cell and the difference between the integral refractive index of the cell per spatial point and the refractive index of the cell surroundings (typically cell medium with a constant refractive index) [16]. Local changes in the cell refractive index along the cell

thickness may occur during various dynamic processes, such as action potential propagation, or by transverse movement of the inner organelles of the cell. Independently or not, geometric path changes can occur due to any morphological change of the cell such as membrane fluctuations and cell swelling. These conjugated parameters, the refractive index difference and the thickness, are not distinct when acquiring the phase profile of a dynamic cell. This fact must be considered during development of the WFDI optical system capturing the cell phase profile and in the quantitative data analysis which follows.

Many morphological parameters which are useful for cell biologists, including cell volume and cell force distribution, are based on the thickness profile of the cell rather than on its phase profile. Various efforts have been performed to decouple thickness from refractive index difference using the cell phase profile. Popescu *et al* [17,18] and Rappaz *et al* [19] have shown that for certain cells, such as red blood cells, in which a constant refractive index can be assumed for the entire cell contents, the thickness profile can be directly obtained from the phase profile. This method, however, is limited to homogenous cell types that do not contain nuclei or other organelles with varying refractive indices. As we demonstrate here, this is not a valid assumption for cardiomyocytes.

Other studies [20–22] have shown that for heterogeneous cells, which contain organelles with different refractive indices, certain parameters such as cell area and dry mass can be obtained directly from the phase profile. In addition, if the cell volume increases in an isotropic way during the cell transient (for example, due to swelling) relative volume can still be calculated in a good approximation [13,21].

If, however, a complete thickness profile is required, more involved experimental measurements are typically employed. Rappaz *et al* [16,19] have used two types of cell media with distinct refractive indices and measured two phase profiles of the same cell. Then, by subtracting the two phase measurements, the cell thickness profile can be obtained. However, this method is effective only if the cell is not highly dynamic and the changes between the consecutive phase measurements are minimal. Alternatively, scanning the cell from different points of view can be used to obtain a refractive index map inside the cell [23,24]. Park *et al* [25] have proposed a system integrating WFDI and epi-fluorescence microscopy, which can in principle detect the organelle locations in real time. Then, if the organelle refractive indices are known in advance, the thickness profile can be obtained. Rappaz *et al* [26] have proposed to simultaneously measure cell thickness and refractive index by using two illumination wavelengths and an extracellular dye to induce an enhanced dispersion of the medium.

Additionally, the conjugation of thickness and refractive index difference in the phase profile can be used in a complementary way: rather than measuring or assuming a certain refractive index and calculating the cell thickness profile, the cell thickness can be measured by another method and then, in combination with the phase measurement obtained by WFDI, used to calculate the refractive indices of the cell organelles. For example, Curl *et al* [27] and Lue *et al* [28] have used confocal microscopy in combination with WFDI microscopy to measure refractive indices of cell organelles, and Edward *et al* [29] have measured the cell height by shear-force feedback topography and combined it with the WFDI-based phase measurement. Another approach is to restrain the cell mechanically to a known thickness in the direction perpendicular to the illumination beam. This can be performed, for example, by attaching another coverslip to the sample [30] or using a dedicated micro-channel device [31]. Kemper *et al* [32], Kemmler *et al* [33], and Tychinsky *et al* [34] have shown that for cells of relatively uniform shape in suspension, the transverse viewable area of the cell can be used to evaluate the cell thickness. For example, if the cell shape is a perfect sphere, its width is equal to its height. In all of these specific cases, as soon as the thickness of the cell is known, the integral refractive index can be calculated using the phase profile obtained by WFDI. These

methods however cannot be used for many eukaryotic cells, including cardiomyocytes, which are terminally differentiated and highly specialized in shape and function.

In this paper, we show that the WFDI-based phase profile is useful for quantitative analysis of cells, even in cases where decoupling of thickness and refractive index is not possible or desired. This is the case for cardiomyocytes, as they contain a significant number of highly dynamic subcellular organelles that are known to have varying refractive indices. First, by using confocal dual-channel fluorescence microscopy, we demonstrate that motion of the subcellular organelles precludes use of a homogenous refractive index assumption. The dynamic behavior of cardiomyocytes is characterized by a rapid contraction of the cell followed by restoration to the resting point. We capture this phenomenon by measuring whole-cell dynamic phase profiles with WFDI, and then analyze these profiles using newly defined numerical parameters. These parameters can be used to quantify specific processes of value to cell biologists, and thus provide a unique non-invasive and label-free approach for studying the impact of different environmental conditions on cardiomyocyte function. We validate the utility of the proposed parameters by showing they are sensitive enough to discriminate modulation of cardiomyocytes contraction dynamics due to temperature change.

2. Cardiomyocyte preparation

For the experiments in this paper, ventricular cardiomyocytes were isolated from two-day old Sprague Dawley rat neonates [35,36]. Briefly, heart ventricle was dissected, minced, and digested in 0.8 mg/ml trypsin (USB Corporation) in Hanks balanced salt solution (HBBS) (Gibco) for 15 hours at 4°C, and then gently dispersed in 200 units/ml collagenase type 2 (Worthington) at 22°C. Cardiac fibroblasts and other adherent cells were removed by two sequential platings in attachment medium for 45 min at 37°C. Cardiomyocytes in suspension were plated at 50% confluency onto glass pretreated with 25 µg/ml fibronectin in phosphate buffered saline (PBS) for 1 hour at 37°C, and then cultured in high-serum medium for 18 hours, followed by low-serum differentiation medium for 48 hours.

Attachment medium was M199 (Gibco), 10% heat-inactivated horse serum (Hyclone), and supplements [10 mM HEPES, pH 7.0, 0.45% (v/v) D-glucose, 0.5 µg/ml vitamin B-12 (Sigma-Aldrich), 0.1 mM MEM non-essential amino acids, 2.0 mM GlutaMAX-I, 100 units/ml penicillin, and 100 µg/ml streptomycin (Invitrogen)]. Low-serum differentiation medium was 2% heat inactivated horse serum (Hyclone) plus supplements. High-serum medium was DMEM/F12, 10% heat inactivated horse serum, 10% calf serum (Colorado Serum Company), 0.45% (v/v) D-glucose, 0.5 µg/ml vitamin B-12 (Sigma-Aldrich), 100 units/ml penicillin, and 100 µg/ml streptomycin (Invitrogen). Live cells were imaged in low-serum differentiation medium.

3. Examination of cardiomyocyte structure by dual-channel fluorescence microscopy

Contrary to cells with homogenous refractive index, cardiomyocytes contain organelles with varying refractive indices distributed across the cell interior. These mainly include myofibrils of highly organized sarcomeric arrays of myosin and actin, nuclei, and mitochondria [2,3]. Using confocal dual-channel fluorescence microscopy, we demonstrate that these organelles of different refractive indices are moving during the entire beating cycle of the cardiomyocyte, which precludes calculating the cell thickness profiles from the phase measurements obtained by one-exposure WFDI during the cell beating cycle.

Prior to the fluorescence imaging, the cells were labeled by two fluorescence dyes simultaneously. We used 5.0 µg/ml Hoechst 34580 (Invitrogen) to image the cell nuclei, and 100 ng/ml MitoTracker Deep Red FM 22426 (Invitrogen) to image the cell mitochondria. The signal from the MitoTracker Deep Red dye was confirmed to be specific to mitochondria by

co-localization with antibody to mitochondrial protein TOMM22 (Abcam) and visualized by immunofluorescence using goat anti-mouse Alexa Fluor 488 (Invitrogen).

For the fluorescence imaging, we used a Leica SP5 confocal microscope and a 100 \times magnification, 1.4 numerical-aperture, oil-immersion objective. For the mitochondria-labeling fluorescent dye, we used a HeNe laser (633nm) as the excitation source and a band-pass emission filter at 640nm-710nm. For the nuclei-labeling fluorescent dye, we used a 405nm laser diode as the excitation source and a band-pass emission filter at 412nm-483nm. Confocal dual-channel fluorescence images were acquired at 13.7 fps.

Figure 1(a) shows the overlaid multi-depth, dual-fluorescence-channel image of several cells in the monolayer, and [Media 1](#) presents the associated cell dynamics. As can be seen,

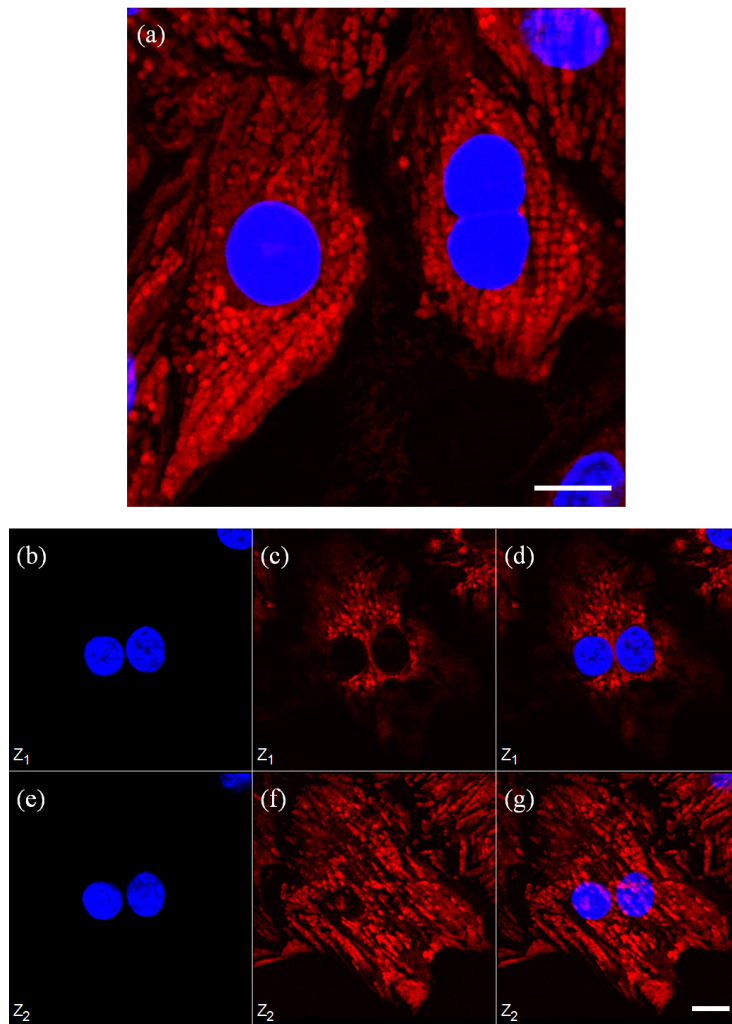


Fig. 1. Tracking the dynamics of the mitochondria (red) and nuclei (blue) during the contraction of live cardiomyocytes, as obtained by confocal dual-channel fluorescence microscopy, 100 \times . (a) Overlaid image of several cells (dynamics, 13.7 fps for 20.2 sec: [Media 1](#)); (b–g) Another cell from the monolayer in two different axial positions, Z_1 (b–d) and Z_2 (e–g) in two time periods (dynamics, 13.7 fps for 20.2 sec: [Media 2](#)), demonstrating the complex structure and dynamics of these cells. (b,e) Nuclei only, (c,f) Mitochondria only, (d,g) Overlaid images. White horizontal scale bars in (a) and in (b–g) represent 10 μ m.

cardiomyocytes typically contain 1 or 2 nuclei per cell and mitochondria that are distributed over the entire cell volume. During beating, the positions of the nuclei showed minor fluctuations, in contrast to the mitochondria which moved in concert with the cell contraction.

Figures 1(b)–1(g) and [Media 2](#) show two confocal depth slices inside another cardiomyocyte. The first confocal slice [Figs. 1(b)–1(d)] was chosen at the depth of the middle of the cell nuclei, whereas the second confocal slice [Figs. 1(e)–1(g)] was chosen at a depth located below the cell nuclei. As can be seen, mitochondria are located even below the cell nuclei and move during the cell beating cycle. In addition, in some cardiomyocytes, the two nuclei are positioned at different depths compared to each other, and both nuclei may fluctuate axially and transversely during contraction. The exact locations and distribution of these organelles vary in different cells in the same monolayer. Thus, in such highly dynamic cells, organelle locations cannot be known precisely without having additional simultaneous knowledge on the exact cell measured.

For these reasons, it is not possible to accurately decouple refractive index from thickness using the phase-measurement of the entire cardiomyocyte obtained only by one-exposure WFDI. In addition, due to the rapid dynamics of these cells, using other approaches, such as tomographic scanning, or the double-exposure method (phase imaging before and after cell medium exchange), can result in loss of dynamic information when recording these cells. Nevertheless, in Section 5 we have identified numerical parameters that are based on the analysis of the entire cardiomyocyte phase profiles obtained by WFDI as explained in Section 4. These parameters do not require decoupling of the cell thickness from its refractive index and constitute a novel phenotypic description of a contractile cell.

4. Recording the phase profiles of cardiomyocytes using WFDI

To obtain the phase profiles of cardiomyocytes by WFDI, more cardiomyocytes were prepared as described in the former section, but not fluorescently labeled this time. Prior to the WFDI imaging, the cardiomyocyte-bearing coverslip was put into a chamber that ensured a constant height of the entire sample, preventing a gradient artifact in the final phase profiles. Single-exposure interferograms were collected with the custom-made off-axis interferometric microscope shown in Fig. 2. Briefly, light from a laser source (17mW, 633nm HeNe) was first spatially filtered and then split into reference and object beams. The object beam was transmitted through the cardiomyocyte sample and magnified by a microscope objective (40× magnification, 0.66 numerical aperture). The reference beam was transmitted through a compensating microscope objective and then combined with the object beam at an angle. The combined beams were projected onto a digital camera (Pike F-032B, AVT, with 640 × 480 pixels of 7.4 μm × 7.4 μm each) by lens L₂, creating a high-spatial-frequency off-axis interferogram of the sample on the camera.

Using the digital camera, we acquired 120 interferograms per second; each interferogram captured the entire amplitude and phase distribution of the light that was transmitted through the sample. Temperature control and micropipettes were integrated to the sample stage to enable measurements of the response of cardiomyocyte cultures to different environmental conditions.

The acquired interferograms were digitally processed, according to the digital processing algorithms which we explained elsewhere [13,37], to yield the quantitative phase profiles of the sample. Figure 3 and [Media 3](#) show the whole-cell phase profile of an individual cardiomyocyte beating cycle, demonstrating the high temporal and spatial resolution obtained by observing this phenomenon by WFDI. As shown in [Media 3](#), the cardiomyocyte beating cycle includes two phases: contraction, in which certain regions in the cell become denser and higher, and recovery, in which the cell returns to the resting point.

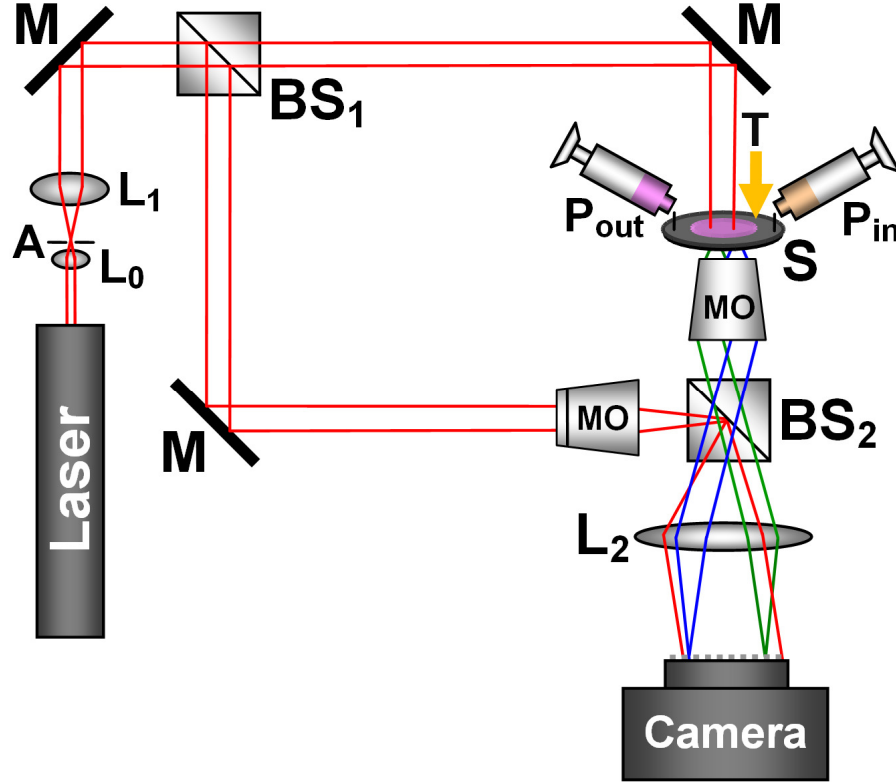


Fig. 2. Off-axis WFDI phase-microscopy system for recording cardiomyocyte dynamics in various environmental conditions. A = Pinhole; L_0 , L_1 , L_2 = Lenses; BS_1 , BS_2 = Beam splitters; M = Mirror; S = Sample; P_{in} , P_{out} = Micro-pipettes; MO = Microscope objective; T = Temperature control.

5. Definitions for numerical analysis on the WFDI-based phase profiles

In order to numerically quantify the dynamic phase profile of the cells, we first define the phase-average displacement (PAD) as follows:

$$\Delta\phi_t(x, y) = \phi_t(x, y) - \phi_0(x, y), \quad (1)$$

where $\phi_t(x, y)$ is the spatially varying phase at time point t , and $\phi_0(x, y)$ is the spatially varying phase at the resting time point of the cell, or, if such time point is not known $\phi_0(x, y)$ is defined as the time average of the entire phase-profile transient $\phi_0(x, y) = \langle \phi_t(x, y) \rangle_t$. Using Eq. (1), we define the positive and negative mean-square phase-average displacements (MS-PAD⁺ and MS-PAD⁻, respectively) as follows:

$$\begin{aligned} \Delta\phi_{MS}^+(x, y) &= \left\langle (\Delta\phi_t(x, y))^2 : \Delta\phi_t(x, y) \geq 0 \right\rangle_t, \\ \Delta\phi_{MS}^-(x, y) &= \left\langle (\Delta\phi_t(x, y))^2 : \Delta\phi_t(x, y) < 0 \right\rangle_t, \end{aligned} \quad (2)$$

and the spectral-domain MS-PAD as follows:

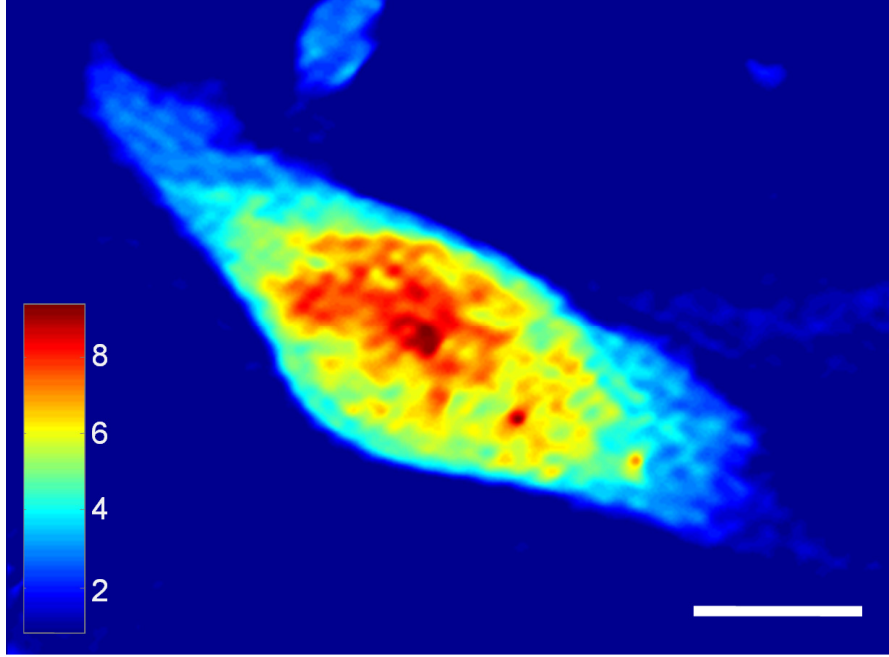


Fig. 3. WFDI-based phase profile of a cardiomyocyte during a single beating cycle, 40 \times . White horizontal scale bar represents 10 μm . Vertical color bar is in radians. Dynamics, 120 fps for 1 sec: [Media 3](#).

$$\Delta\phi_{MS}(f_x, f_y) = \left\langle \left| \Delta\phi_t(f_x, f_y) \right|^2 \right\rangle_t, \quad (3)$$

where $\Delta\phi_t(f_x, f_y)$ is obtained by a spatial Fourier transform of $\Delta\phi_t(x, y)$. Using Eqs. (2) and (3), we define the following parameters to describe the MS-PAD global contributions:

$$\eta_1^+ = \sqrt{\left\langle \Delta\phi_{MS}^+(x, y) \right\rangle_{(x,y)}}, \quad \eta_1^- = \sqrt{\left\langle \Delta\phi_{MS}^-(x, y) \right\rangle_{(x,y)}}, \quad \eta_2 = \sqrt{\left\langle \Delta\phi_{MS}(f_x, f_y) \right\rangle_{(f_x, f_y)}}, \quad (4)$$

where $\langle \bullet \rangle_{(x,y)}$ and $\langle \bullet \rangle_{(f_x, f_y)}$ define an area averaging.

Let us also define the phase instantaneous displacement (PID) as follows:

$$\Delta\phi_{t,\tau}(x, y) = \phi_{t+\tau}(x, y) - \phi_t(x, y). \quad (5)$$

where τ defines the time duration between time point t and time point $t + \tau$. Using Eq. (5), we define the positive and negative mean-square phase instantaneous displacements (MS-PID⁺ and MS-PID⁻, respectively) as follows:

$$\begin{aligned} \Delta\phi_{MS,\tau}^+(x, y) &= \left\langle \left(\Delta\phi_{t,\tau}(x, y) \right)^2 : \Delta\phi_{t,\tau}(x, y) \geq 0 \right\rangle_t, \\ \Delta\phi_{MS,\tau}^-(x, y) &= \left\langle \left(\Delta\phi_{t,\tau}(x, y) \right)^2 : \Delta\phi_{t,\tau}(x, y) < 0 \right\rangle_t, \end{aligned} \quad (6)$$

as well as the spectral-domain MS-PID as follows:

$$\Delta\phi_{MS,\tau}(f_x, f_y) = \left\langle \left| \Delta\phi_{t,\tau}(f_x, f_y) \right|^2 \right\rangle_t, \quad (7)$$

where $\Delta\phi_{t,\tau}(f_x, f_y)$ is obtained by a spatial Fourier transform of $\Delta\phi_{t,\tau}(x, y)$. By using Eqs. (6) and (7), we define parameters describing the MS-PID global contributions:

$$\gamma_{1,\tau}^+ = \sqrt{\left\langle \Delta\phi_{MS,\tau}^+(x, y) \right\rangle_{(x,y)}}, \quad \gamma_{1,\tau}^- = \sqrt{\left\langle \Delta\phi_{MS,\tau}^-(x, y) \right\rangle_{(x,y)}}, \quad \gamma_{2,\tau} = \sqrt{\left\langle \Delta\phi_{MS,\tau}(f_x, f_y) \right\rangle_{(f_x, f_y)}}. \quad (8)$$

As the cell phase profile is strongly associated with its dry mass [20–22], the parameters defined above are associated with motion of different cell structures including subcellular organelles. For example, the spectral-domain MS-PID has been used to describe cancer cell dynamics [21]. Note that all the parameters defined above are based on the entire phase-profile transient, without the need to extract the thickness profile first.

6. WFDI-based numerical analysis of cardiomyocyte dynamics

As shown in this section, the analysis tools described above are sensitive enough to detect the subtle changes in the dynamic phase profile of a beating cardiomyocyte occurring due to temperature decrease. As shown in Fig. 2, a custom temperature control was integrated into the sample stage in the interferometric system to enable this study. Figures 4(a) and 4(e) compare the phase profiles of the same cell shown in Fig. 3 during a single beating cycle at 30°C and 23°C, respectively. As can be seen in Media 4, the cell in Fig. 4(e) tends to show more motion along a greater segment of its length in comparison to the cell shown in Fig. 4(a), especially in the recovery stage, which we define as the time interval between the point of maximum stretch of the cell and the point when the cell returned to the resting stage. The relatively slow recovery phase observed at lower temperatures is consistent with temperature-induced inhibition of calcium-regulated contraction, as discussed at the end of this section.

The dynamic differences during the beating cycle of the same cell at 30°C in comparison to 23°C are more obvious from the PAD and PID profiles shown in Figs. 4(b)–4(d), 4(f)–4(h)

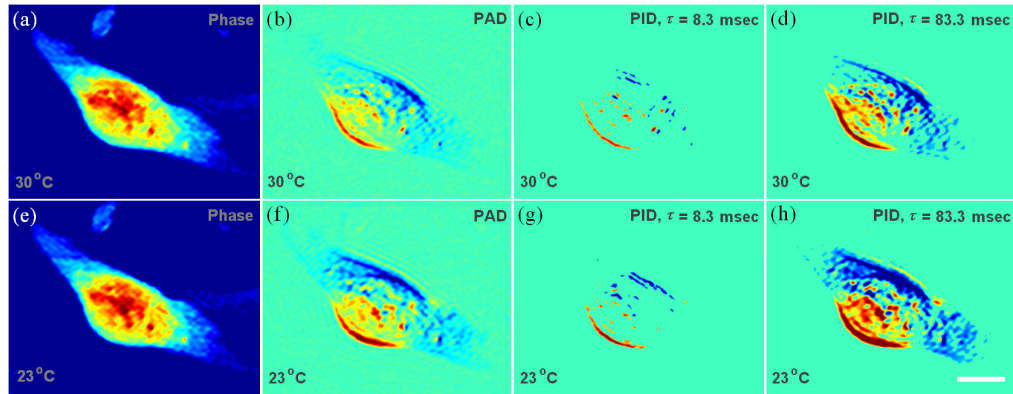


Fig. 4. Example of numerical analysis applied on a WFDI-based phase profile of a cardiomyocyte during beating at two different temperatures: (a–d) at 30°C, (e–h) at 23°C. (a,e) Phase profile; (b,f) PAD profile; (c,g) PID profile for $\tau = 8.3$ msec (one-frame separation); (d,h) PID profile for $\tau = 83.3$ msec (ten-frame separation). In (b–d,f–h): ‘hot’ colors represent positive values, ‘cold’ colors represent negative values, and cyan represents zeros. White horizontal scale bar represents 10 μm . Dynamics, 120 fps for 1 sec: Media 4.

(see Media 4). As seen in Figs. 4(b) and 4(f), in cardiomyocytes the PAD profiles provide a means of tracking the differential changes in the current WFDI phase profile compared to the associated phase profile in the cell resting point, as defined by Eq. (1), revealing the dry-mass movement inside the cell. Thus, the PAD profiles can be used to study the cell function during the beating cycle. Furthermore, the global contribution of the dynamic PAD profiles is the basis for the MS-PAD profiles that are described by the single-value η parameters which numerically characterize the entire cell beating cycle.

As can be seen in Figs. 4(c), 4(d), 4(g) and 4(h), the PID profiles give an indication of the instantaneous movement of dry mass in the cell associated with organelles of different sizes over different time periods during the cell beating cycle, as defined by the time parameter τ . The subtraction operation defined by Eq. (5) creates a differential measurement between the current phase profile and a previous phase profile, depending on τ , and thus cancels contributions from this previous frame, and reveals uncorrelated regions between the two frames. The MS-PID profiles are calculated based on the dynamic PID profiles, eventually yielding the single-value γ parameters characterizing the cell over various time periods during its transient.

Figures 5(a), 5(b) and Figs. 5(c), 5(d) show the MS-PAD profiles obtained for the dynamic PAD profiles shown in Figs. 4(b) and 4(f) at 30°C and 23°C, respectively. These MS-PAD profiles were used to calculate the η parameters as defined by Eq. (4), and for this particular cell yielded $\eta_1^+ = 0.10998$ and $\eta_1^- = 0.10941$ at 30°C, and $\eta_1^+ = 0.10249$ and $\eta_1^- = 0.10251$ at

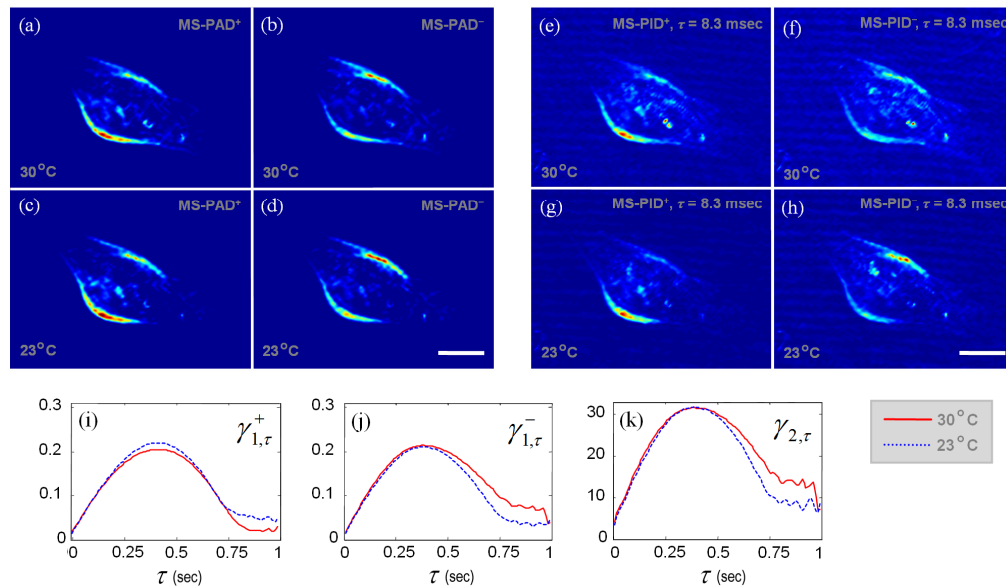


Fig. 5. Calculation of different numerical parameters based on the dynamic phase profiles shown in Fig. 4. (a–d) MS-PAD profiles (based on which the η parameters are defined): (a) MS-PAD⁺ at 30°C (which yields $\eta_1^+ = 0.10998$); (b) MS-PAD⁻ at 30°C (which yields $\eta_1^- = 0.10941$); (c) MS-PAD⁺ at 23°C (which yields $\eta_1^+ = 0.10249$); (d) MS-PAD⁻ at 23°C (which yields $\eta_1^- = 0.10251$). (e–h) MS-PID profiles for $\tau = 8.3$ msec (varying τ : Media 5): (e) MS-PID⁺ at 30°C; (f) MS-PID⁻ at 30°C; (g) MS-PID⁺ at 23°C; (h) MS-PID⁻ at 23°C. (i–k) Graphs showing the dependency of the γ parameters on τ . Solid red lines represent the measurements done at 30°C. Broken blue lines represent the measurements done at 23°C. (i) $\gamma_{1,\tau}^+$ (which is based on MS-PID⁺); (j) $\gamma_{1,\tau}^-$ (which is based on MS-PID⁻); (k) $\gamma_{2,\tau}$ (which is based on the spectral-domain MS-PID). The white horizontal scale bars represent 10 μm .

23°C. In a similar way, the associated spectral-domain PAD profile yielded $\eta_2 = 16.8186$ at 30°C and $\eta_2 = 16.1487$ at 23°C.

Figures 5(e), 5(f) and Figs. 5(g), 5(h) show the MS-PID profiles for $\tau = 8.3$ msec (one frame of separation at 120 fps) at 30°C and 23°C, respectively. Media 5 presents the associated dynamic MS-PID profiles as a function of the time parameter τ . Based on these dynamic MS-PID profiles and on the spectral domain MS-PID profile, we calculated the γ parameters as defined by Eq. (8). Figures 5(i)–5(k) show the dependency of the various γ parameters on τ at the two temperature levels. As can be seen from these graphs, the difference between the two temperature levels is more pronounced for higher τ values than for lower τ values. This result is expected due to the fact that the change between the two temperature levels is more pronounced in the recovery phase of the cardiomyocyte beating cycle.

The numerical analysis described above was performed on the WFDI phase profiles of 18 individual cardiomyocytes at 30°C. The values obtained for each of the γ and η parameters were averaged over 3–4 beating cycles and normalized by the viewable area of the cell. Afterwards, the experiments were repeated at 23°C. Figure 6 summarizes the results obtained. Statistical significance between the two groups of cells (at 30°C and at 23°C) were seen for all γ and η parameters, as indicated by the low p -values (calculated by the two-sided Wilcoxon rank-sum test [38]). These results demonstrate that the unique whole-cell-based numerical parameters defined in this paper can be used to discriminate between different dynamic behaviors of cardiomyocytes, and thus can be used to quantitatively study on dynamic phenomena in these cells.

As can also be seen in Fig. 6, there is an apparent advantage for using the negative parameters $\gamma_{i,\tau}^-$ for discriminating between the two groups of cells. Higher values in these parameters represent increased levels of MS-PID⁻. In the recovery phase of the cell, it is more likely to have more cell points with negative MS-PID than positive MS-PID, since the phase profile in the cell contractile region decreases. This implies that there is a larger influence of the ambient temperature in the recovery phase of the cell beating cycle, as compared to the contraction phase.

These results are supported by previous studies performed by other methods, where temperature had a profound effect on the biochemistry of contraction in the myocardium of the intact heart and in cardiomyocytes *in vitro*. In classic work, the force of isometric contraction of the myocardium in warm-blooded animals rose as temperature was lowered from 37°C to 20°C, a trend that was also seen in myocardium of cold-blooded animals to near freezing temperatures [39]. In addition, both velocity of contraction and the time taken to achieve maximal force were depressed by the cold [40]. Calcium regulates contraction of the myocardium [41] and shows profound temperature sensitivity particularly below 21°C in vertebrates. For example, in adult rat ventricular cardiomyocytes *in vitro*, the propagation of calcium waves (recorded by fluorescence labeling), including rise and decay, decreased markedly at lower temperatures [42]. Likewise, the kinetics of calcium sparks in rat cardiomyocytes were found to be temperature dependent, slowing significantly due to prolonged calcium release, indicating a possible link between temperature and contraction recovery [43]. Remarkably, the frequency of calcium-regulated contractile events in rat cardiomyocytes is relatively consistent between 37°C and 30°C, but shows significant difference between 30°C and lower temperatures [42,43]; thus, for the current study, cardiomyocytes were imaged at 30°C and 23°C.

A possible mechanism for the temperature dependence of actin-activated myosin ATPase was presented recently in a theoretical model showing that myosin moved in a unidirectional Brownian motion along the actin filament. In the model, both the energy of

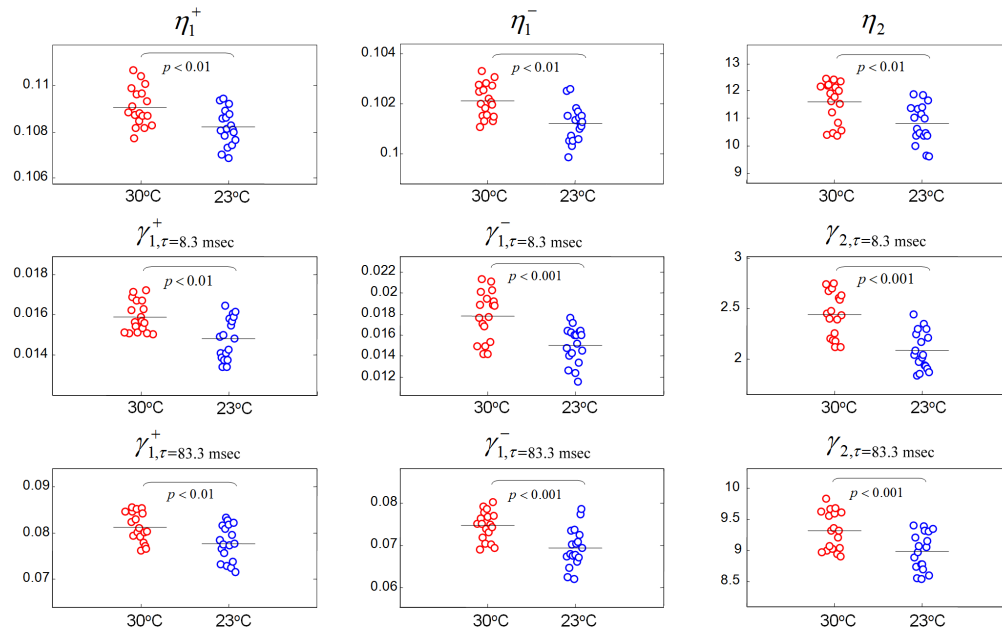


Fig. 6. Values of the γ and η parameters that are based on the whole-cell phase profiles, demonstrating that these parameters discriminate between cardiomyocytes beating at 30°C and 23°C (18 cells in each group, 3-4 beating cycles per each cell). Each circle represents a different cardiomyocyte, and the horizontal line at each group represents the average value for all cells in the group.

adenosine-5'-triphosphate (ATP) hydrolysis and random thermal noise were used to modify the local energy landscape to perform the work of contraction [44].

To the best of our knowledge, the current paper is the first time that a numerical analysis has been performed on label-free WFDI phase profiles of live cardiomyocytes at 120 fps, taking into consideration the entire three-dimensional shape and refractive index changes during the cardiomyocyte contraction at different temperatures. The whole-cell analysis tools presented in this paper capture intermediate events associated with dry-mass movement over different time frames during the cardiomyocyte beating cycle. These intermediate events cannot be well discriminated by directly visualizing the dynamic phase profiles of the cell. In contrast, the single-value η and γ parameters can uniquely characterize the cell function, as demonstrated for temperature change. We believe that these numerical tools can be useful for analyzing various fast dynamic behaviors in other biological cells, including intra- and extra-cellular membrane fluctuations and reorganization of the cell cytoskeleton.

7. Conclusion

We have used WFDI phase microscopy to study the three-dimensional dynamics of cardiomyocytes *in vitro*, where no exogenous contrast agents or sample preparation are needed, and the acquisition frame rate is equal to the maximal camera frame rate. As demonstrated by confocal fluorescence microscopy, cardiomyocytes contain complex organelles of various refractive indices that are distributed throughout the cell cytoplasm and move rapidly during the entire cell beating cycle. For this reason, it is not possible to use the constant refractive index assumption to calculate the thickness profile of the cell based on the single-exposure WFDI-based phase profile. Therefore, we have defined new numerical-

analysis tools that can be used to study the whole-cell phase-profile dynamics, and have utilized them to analyze cardiomyocyte phase profiles acquired during cell beating cycles. We have demonstrated that these numerical tools are sensitive enough to discriminate changes in the cardiomyocyte function in response to changes in temperature, and thus represent novel means to quantify cellular phenotype-associated dynamics. In fact, these results show that whole-cell WFPI phase microscopy is a superior approach for wide-field imaging of contractile cells, due to the ability of the technique to obtain numerical parameters without using any type of exogenous labeling or scanning. Significantly, this approach can be used even for cells that possess an inherently complex refractive-index and three-dimensional structure that changes over time. We anticipate that the tools presented in this paper will provide a unique non-invasive, label-free and scan-less method to assess the impact of genetic mutations, environmental influences, and potential therapeutics on cardiomyocyte function.

Acknowledgments

This work was supported by National Science Foundation (NSF) grant CBET-0651622. N.T.S. greatly acknowledges the support of the Bikura Postdoctoral Fellowship from Israel. The authors thank Dr. George Truskey for advice and support, Dr. Yasheng Gao for his advice regarding the confocal fluorescence microscopy experiments, and Ava Kroll for isolating the cardiomyocytes.